Engineering Geology 369 (2026) 108813

Contents lists available at ScienceDirect

Engineering Geology

journal homepage: www.elsevier.com/locate/enggeo

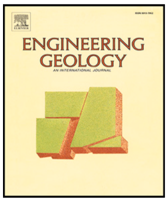

Dynamic particle fragmentation modulates friction evolution and shear mobility in dry granular flows

Haodong Gao [a,b], Shun Wang [a,b,*], Ruijun Wang [a,b], Xuan Kang [c], Jidong Zhao [d]

[a] State Key Laboratory of Water Resources Engineering and Management, Wuhan University, Wuhan, 430072, China
[b] Institute of Engineering Risk and Disaster Prevention, School of Water Resources and Hydropower Engineering, Wuhan University, Wuhan, 430072, China
[c] Institute of Geotechnical Engineering, Department of Structural Engineering and Natural Hazards, University of Natural Resources and Life Sciences, Vienna, A-1180, Austria
[d] Department of Civil and Environmental Engineering, The Hong Kong University of Science and Technology, 999077, Hong Kong, China

ARTICLE INFO

Dataset link: Particle dynamic fragmentation regulates friction and mobility in geophysical flows (Original data)

Keywords:
Granular materials
Particle fragmentation
Shear localization
Frictional weakening
Visual analysis

ABSTRACT

Shear localization and particle fragmentation in granular materials affect the friction behavior and mobility of catastrophic mass flows such as landslides and rock avalanches. However, existing studies commonly describe localization qualitatively or in 2D, limiting objective tracking of shear zone and micro–macro linkage to friction transitions. This study provides a microscopic mechanism to unravel how fragmentation and localization regulate granular friction. Combining ring shear experiments, X-ray computed tomography, and microstructure analysis, we systematically investigate the dynamic shear response of three contrasting granular materials, including crushable quartz sand, halite, and non-crushable glass beads, under controlled normal stresses, shear velocities, and displacements. The friction response follows a three-stage evolution featuring two distinct shear resistance peaks: an initial transient shear stage marked by force chain mobilization and early grain interlocking, a strengthening stage driven by progressive compaction and limited fragmentation, and a weakening stage dominated by intense particle breakage, shear zone development, and the rolling of spheroidized fine grains. This evolution is quantitatively linked to particle-scale processes, enabling parameterization of the peak-to-residual transition for theoretical formulations and mobility prediction. This study further introduces a new analytical approach based on solid fraction fluctuations to characterize shear localization dynamics and to enable localized 3D breakage quantification. The results reveal that crushable materials exhibit rapid fragmentation and pronounced friction weakening, while non-crushable systems maintain a stable rolling-dominated regime. These findings advance the understanding of how particle breakage, morphology, and localization interact to control granular rheology and support predictive modeling of dense granular flows in natural hazard contexts.

1. Introduction

Granular materials are ubiquitous in geological environments and constitute the primary components of many catastrophic mass flows including landslides, rock avalanches, and debris flows (Locat et al., 2003; Baumberger and Caroli, 2006; Bian et al., 2024). These flows frequently exhibit catastrophic ultramobility, achieving runout distances far exceeding predictions based on initial potential energy. Typical examples include the 2014 Oso landslide (Washington, USA), which traversed over 1 km in approximately two minutes, destroying 49 structures and claiming 43 lives (Wartman et al., 2016), and the Aoraki/Mt. Cook rock avalanche (New Zealand), which transported more than 7 million cubic meters of rock over 7 km within minutes (McSaveney and Davies, 2007; Dunning and Armitage, 2010). Dynamic fragmentation of granular material during long-runout motion is recognized as a key mechanism governing this catastrophic ultramobility. The continuous mechanical fragmentation of coarse grains into finer fractions that form lubricating layers within shear zones, fundamentally alters the flow rheology and enhances the overall mobility of rock avalanches (Furuki and Chigira, 2019; Cabrera and Estrada, 2021; Pudasaini et al., 2024). Proposed mechanisms for this ultramobility include thermal pressurization, acoustic fluidization, and dynamical fragmentation (Melosh, 1986; Brantut et al., 2008). In dense granular physics, the classic $\mu(I)$ rheology (Jop et al., 2006) explains

---

[*] Correspondence to: State Key Laboratory of Water Resources Engineering and Management, Wuhan University, Bayi Road, Wuchang, Wuhan 430072, China.
E-mail addresses: gaohaodong955@whu.edu.cn (H. Gao), shun.wang@whu.edu.cn (S. Wang), ruijunwang@whu.edu.cn (R. Wang), xuan.kang@boku.ac.at (X. Kang), jzhao@ust.hk (J. Zhao).
URL: https://swrh.whu.edu.cn/info/1623/10136.htm (S. Wang).

https://doi.org/10.1016/j.enggeo.2026.108813
Received 6 January 2026; Received in revised form 1 April 2026; Accepted 10 May 2026
Available online 15 May 2026

frictional reduction through a decreased inertial number as particles fragment and shrink. However, under high-stress confined shear, this rate-dependent frictional reduction is dynamically co-governed by localized structural reorganizations. Consequently, understanding the dynamic response of granular materials under varying shear conditions and how particle fragmentation influences shear resistance and microstructure is crucial for predicting disaster impacts and developing effective mitigation strategies.

The fragmentation process of granular material during shearing is governed by both extrinsic mechanical conditions (e.g., loading conditions, shear velocity, and loading history) and intrinsic material properties (e.g., initial fracturing, grain size, and mechanical characteristics such as compressive strength, and fracture toughness) (Zhao et al., 2015). Fragmentation typically initiates at inherent flaws when the local yield strength is exceeded, leading to particle failure. This phenomenon is critically linked to the pronounced frictional weakening and enhanced mobility observed in catastrophic mass flows, such as long-runout landslides and seismic fault slip (Davies and McSaveney, 2009; Jiang et al., 2016; Wang et al., 2021). However, while significant progress has been made in understanding granular shear response, critical limitations persist. Experimental studies using ring-shear devices have demonstrated that fragmentation induced fines generation promotes weakening through powder lubrication in crushable materials (e.g., quartz sand), whereas non-crushable systems (e.g., glass beads) maintain stable strength via geometric rearrangement (De Paola et al., 2015; Green et al., 2015; Cai et al., 2019). Numerical simulations have further revealed that the initial particle size distribution (PSD), loading rate, and stress conditions collectively regulate the dynamic fragmentation process (Wang and Wang, 2022; Du et al., 2024). Theoretically, various constitutive models incorporating particle breakage have been developed to describe evolving mechanical properties (Einav, 2007; Collins-Craft et al., 2020; Tang et al., 2024; Wang et al., 2024). However, prevailing studies remain constrained by short shear displacements and low stress conditions, failing to replicate the intense, prolonged fragmentation and microstructural evolution characteristic of natural ultramobile flows. These limitations impede a mechanistic understanding of how progressive fragmentation governs the transition from peak strength to sustained weakening and ultimately controls flow mobility.

In many geophysical flows, shear deformation and particle fragmentation exhibit pronounced localization, and this behavior differs fundamentally from the globally fragmentation typically observed in conventional triaxial or compression tests. Sliding shear motion becomes concentrated in relatively narrow shear zones, with the dynamic evolution of these zones governing flow mobility and displacement (Furuki and Chigira, 2019; Kang et al., 2025). Consequently, shear localization and microstructural evolution in granular materials have long been points of research focus in fields such as landslide dynamics. Several researchers have observed the development of shear zones during slip processes by using advanced transparent shear boxes, combining optical and scanning electron microscopy (SEM) techniques to examine microstructural changes in thin sections of shear zones. For instance, Fukuoka et al. (2007) used a ring shear apparatus with a transparent shear box to directly observe the evolution of shear zones and granular material motion, Crosta et al. (2007) used photographic and optical techniques to describe particle segregation in post-avalanche deposits, and Wei et al. (2021) used optical microscopy to obtain two dimensional (2D) projected particle images in order to analyze particle fragmentation during shear. However, those studies were focused primarily on qualitative or 2D analyses, with limited research on the dynamically spatial variations of granular materials, and in particular the quantification of shear affected areas was challenging. Recent advances in X-ray computed tomography (CT) have enabled non-destructive visualization of shear zone evolution, revealing local particle rearrangement and fracture patterns. Some researchers have used CT scanning to investigate the grain-scale behavior of granular materials and the evolution of interparticle contact structures (Alikarami et al., 2015; Wang et al., 2022). However, despite these advancements, existing analyses often rely on bulk measurements that obscure localized deformation mechanisms, such as the formation of fine particle-rich shear interfaces observed in natural fault zones.

Furthermore, a critical gap persists in bridging microscale fragmentation dynamics to macroscale shear responses. First, conventional methods struggle to quantify real-time particle fragmentation and its spatial heterogeneity in shear zones. While discrete element modeling can simulate force-chain evolution, it often oversimplifies particle breakage criteria and fails to replicate the progressive rounding of fine particles observed experimentally (Du et al., 2024). Second, few laboratory studies have tracked the evolution of sphericity during shearing, leaving the interactions among particle sphericity, lubrication by fines, and frictional transitions unresolved. Third, existing criteria for defining shear zone boundaries often oversimplify the interplay between particle fragmentation and shear localization. Traditional experimental techniques, such as optical strain mapping or post-slip grain size analysis struggle to capture the transient thickening or thinning of shear zones under high stress because of experimental hysteresis (Niemeijer and Spiers, 2007). Collectively, these limitations hinder the development of constitutive models that can predict more accurately the dynamic transition from brittle fragmentation to fluidization.

The study reported herein integrates high-speed ring shear tests, CT visualization, and SEM in order to investigate the behavior of granular material systematically. Under controlled normal stress (50–400 kPa), shear velocity (0.001–0.1 m/s), and displacement (0.1–100 m), three distinct material types were examined: crushable quartz sand, highly friable halite, and non-crushable glass beads. One of the key contributions is the introduction of an in-situ 3D method based on solid fraction fluctuation, offering a viable avenue to estimate the steady shear-affected zone and observe concurrent particle morphology changes. By correlating macroscopic friction with microstructural evolution, this study quantitatively reveals the transition from interlocking-dominated strengthening to fragmentation-driven weakening. This theoretical mechanism bridges microscale fracture and macroscopic response, offering valuable insights into the ultramobility of catastrophic mass flows and informing predictive models for geological hazards.

2. Materials and methods

2.1. Granular materials

Dry, uniformly graded crushable quartz sand was selected as the primary material to investigate the effects of fragmentation on shear behavior. For comparative analysis, two contrasting materials were also tested: highly friable angular halite (NaCl) and glass beads that exhibit negligible breakage under the study's conditions [Fig. 1(c–e)]. All materials had an initial grain size of 1–2 mm (less than 10% of the sample dimension). This uniform sizing promotes significant fragmentation in the material and facilitates precise assessment of particle size variations. The quartz sand originated from rock weathering processes, including fracturing, transport, and erosion; it had a specific gravity of 2.66, a silicon dioxide (SiO_2) content exceeding 99.6%, a compressive strength of 250 MPa, and a Mohs hardness of 7.5. Despite its high hardness and compressive strength, its angularity, low fracture toughness, and internal defects make it highly susceptible to shear-induced fragmentation. In comparison, the glass beads (specific gravity of 2.52, compressive strength of 220 MPa, and Mohs hardness of 6–7) feature a spherical, homogeneous structure that effectively mitigates stress concentrations and resists breakage. It should be clarified that while not intended to simulate complex natural geomaterials, the glass beads serve as a standard, low-crushability reference to effectively isolate the specific impact of fragmentation on macroscopic frictional

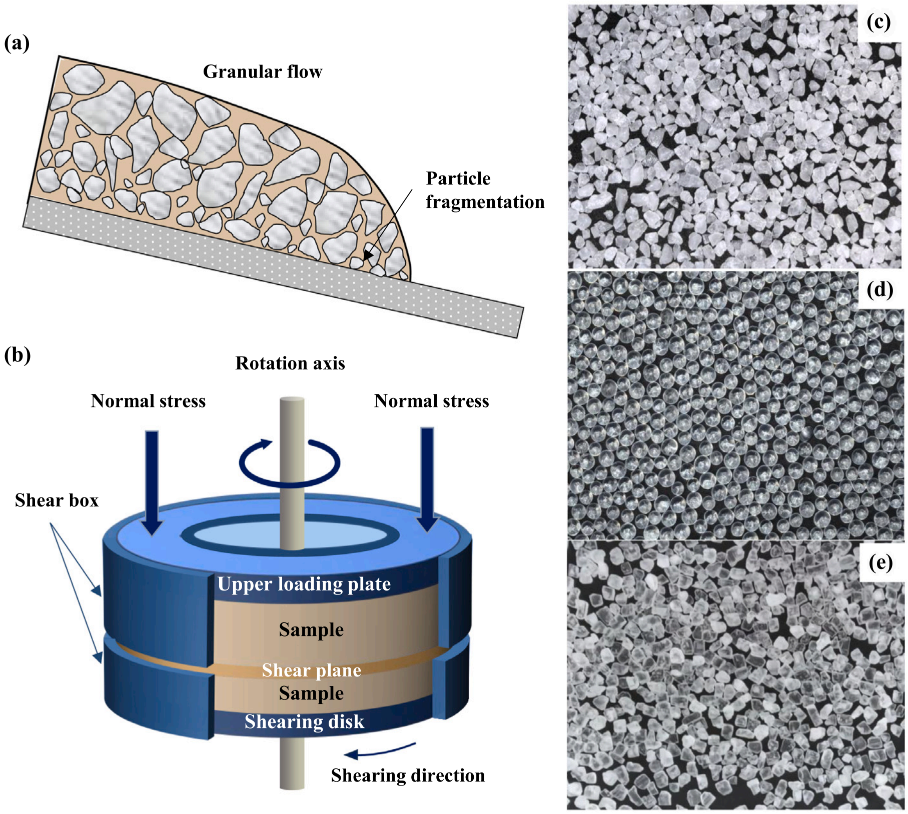

Fig. 1. High-speed ring shear test: schematic of (a) particle flow and (b) ring shear test; (c) quartz sand, (d) glass beads, and (e) halite for testing.

weakening. The halite grains that were used as another test material, were a typical chemically deposited mineral with a specific gravity of 2.1, and a Mohs hardness of 2–2.5, marking it a more readily crushable granular material.

2.2. Ring shear test

Ring shear tests are used widely to investigate the mechanical behavior of geomaterials during large-deformation shear processes, particularly the particle fragmentation characteristics of granular materials under long-distance shear [Fig. 1(a)]. The fundamental principle of the ring shear apparatus involves applying normal stress and torsional shear force to induce relative shearing along a fixed circumferential shear plane until a target state is reached, as shown schematically in Fig. 1(b). This study used the ICL-2 undrained high-speed ring shear apparatus, one of the most advanced ring shear systems developed in recent years [Fig. 2(a)]. The apparatus consists of a main ring shear apparatus, control unit, computer systems, and a power supply box (Sassa et al., 2014). The components of the main ring shear apparatus are detailed in Fig. 2(b)–(g).

The main ring shear apparatus consists of upper and lower shear boxes. The contact interface of the shear boxes is lined with rubber edges, ensuring a sealed environment under conditions of high stress. The apparatus can apply a maximum normal stress of 1 MPa and achieve a maximum shear velocity of 0.5 m/s. The shear box has an outer diameter of 142 mm and an inner diameter of 100 mm, with a shear-participating sample height of 42 mm in this study and a maximum filling height of 50 mm. To ensure a uniform initial filling density, the sample with a given mass was divided into three layers and preliminarily compacted using a small tamper, with each layer approximately 14 mm thick. Before adding each successive layer, the surface of the previous layer was scraped to avoid artificial particle alignment and shear plane formation. The initial solid fraction η of the samples, defined as the ratio of the actual particle volume to total sample volume, was 0.54 and was maintained consistently across all tests. At the outset of the test, the samples were compacted further under the specified normal stress until the axial displacement stabilized. Next, the upper shear box remained stationary while the lower one initiated rotational shearing at the designated shear velocity, continuing until the target shear displacement was reached. To enhance clarity, a simple demonstration animation is provided in the Supplementary Material. For each test, data on normal stress, shear resistance, and axial and shear displacements were recorded for analysis into material responses under various loading conditions. This study examined four normal stress levels (50, 100, 200, and 400 kPa), three shear velocities (0.001, 0.01, and 0.1 m/s), and four shear displacements (0.1, 1, 10, and 100 m). The experimental conditions were designed to approximate the stress conditions inferred for sliding zones at depth. A detailed experimental scheme is provided in Table 1. The normal and shear stress measurements were corrected using the method proposed by Loi et al. (2023).

2.3. Microstructure observations

The sheared quartz sand mixtures were carefully collected using a small-scale industrial vacuum cleaner, after which the particle size distribution was analyzed with a laser particle analyzer, and the textures and surface characteristics of the fractured particles were examined via SEM. Furthermore, X-ray computed tomography (CT) was used in this study to track and visualize the evolution of particle fragmentation under different shear displacements. To preserve the intact structure of the quartz sand samples, a custom-made arc-shaped glass collector was designed independently. The collector has a height of 50 mm, inner and outer diameters of 100 mm and 142 mm, respectively, with an average arc length of 48 mm and radial thickness of 21 mm, precisely matching the shape enclosed by two adjacent serrations at the end of

Fig. 2. Undrained high-speed ring shear apparatus used in this study: (a) device composition; (b) lower shear box; (c) upper shear box; (d) sample setting process; (e) connection to normal stress loading system; (f) hanging frame for lifting of loading cap; (g) position of shearing plane during test.

the shear box. The detailed design content is shown in Fig. S1 of the Supplementary Material. Its thin-wall design minimizes elastic deformation, allowing it to fit seamlessly within the annular shear box. The upper and lower surfaces of the collector are equipped with detachable acrylic sheets. Upon completion of the ring shear testing, the collector's cutting edge was inserted into the quartz sand specimen, while excess material along the container periphery was gradually eliminated. This process ensured that the collector penetrated to the bottom of the shear box with minimal disturbance to the microstructure of the shear zone. For enhanced structural integrity, an epoxy resin adhesive (LOCTITE EA 9483) with high thermal conductivity was used for impregnation. Concurrently, to prevent adhesive clogging of the porous stone and drainage conduits at the shear box base, a polyethylene barrier film was pre-positioned at the bottom prior to sample installation. Post-curing, the specimen assembly was secured with a glass cover plate and subjected to CT scanning at the central region using a GE Phoenix Nanotom S system for internal structural characterization. Each sample generated 1100-1300 CT slices with a spatial resolution of 25 μm. Prior to three-dimensional (3D) reconstruction, the raw CT images underwent essential pre-processing, including noise filtering and contrast enhancement, to optimize image quality. Subsequently, a hybrid segmentation approach combining the Otsu method with manual threshold adjustments was applied to accurately isolate the solid particles from the void spaces (Gao et al., 2024). Using these segmented slice data, 3D reconstruction of the sheared samples was performed via volume rendering, enabling the quantitative analysis of granular morphology parameters. The test procedures are illustrated in Fig. 3, and Table 1 summarizes the specific details of the tests conducted.

3. Test results

3.1. General shear behavior

3.1.1. Effect of normal stresses

At a constant shear rate of 0.01 m/s, quartz sand was sheared up to 100 m under varying normal stresses, and the mechanical response is detailed in Fig. 4. Given the discreteness of granular materials, the particle contact configurations evolve continuously throughout the shear process to accommodate shear deformation, leading to fluctuations in shear resistance. A reliable explanation is that the stress fluctuations within the particle system are attributed primarily to the fragmentation and reconstruction of internal force chains during the particle flow, as well as interparticle collisions (Jiang et al., 2016; Niu et al., 2024). At the onset of shearing, strong interlocking and friction between particles generate an initial peak in shear resistance, followed by a rapid decline (Wang and Huang, 2023), marking a transient stage. During steady state shear, the shear resistance increases with displacement until reaching a maximum, after which it declines gradually to a relatively stable value. For clarity, the key shear resistance parameters are defined as follows [Fig. 4(a)]: τ_p and τ_s are the peak and residual

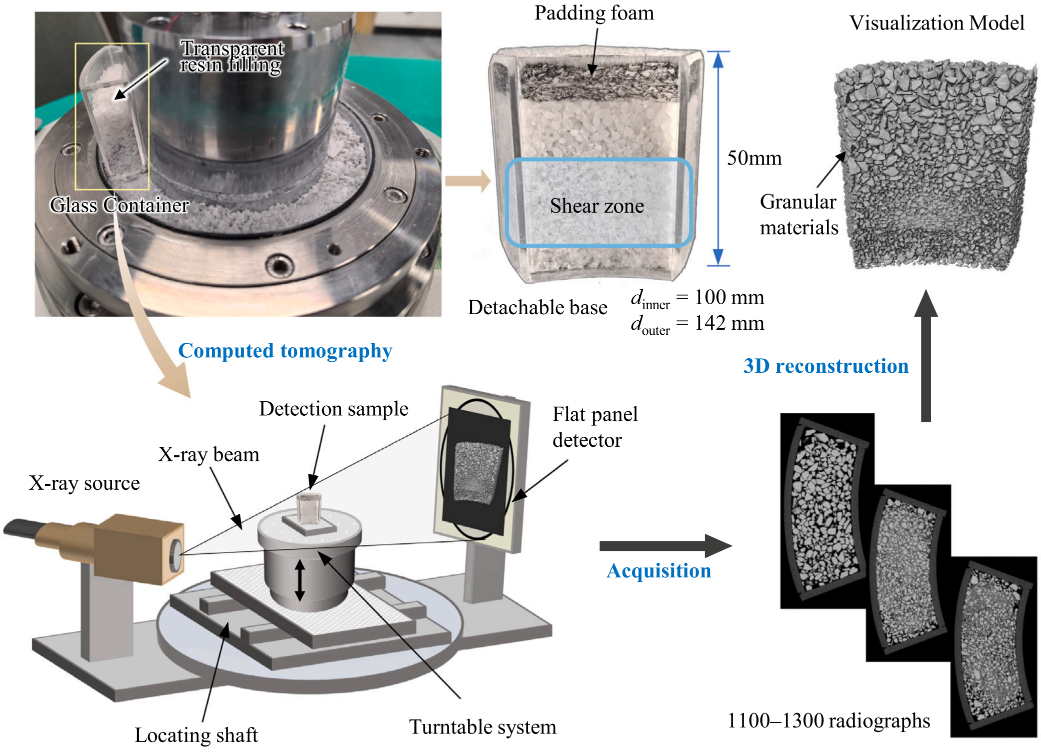

Fig. 3. Representative unit sampling and microstructure visualization process.

Table 1
Summary of test details.

Test	Material	Test conditions	Number of samples	Corresponding standard or source	Test parameters
Ring-shear test	Quartz sand	Normal stress, σ_n: 50, 100, 200, 400 kPa; shear velocity, v: 0.001, 0.01, 0.1 m/s; shear displacement, δ_s: 0.1, 1, 10, 100 m	11	Loi et al. (2023); ISO 17892-10 (2018)	Test filling height: 42 mm; layered compaction, each layer thickness: 14 mm; initial solid fraction: 0.54
	Glass bead	σ_n: 50, 100, 200, 400 kPa; v: 0.01 m/s; δ_s: 100 m	4		Initial solid fraction: 0.57
	Halite grain	σ_n: 50, 100, 200, 400 kPa; v: 0.01 m/s; δ_s: 100 m	4		Initial solid fraction: 0.56; Ambient temperature 20°C, relative humidity 35%
SEM test	Quartz sand	Mixed quartz fragments after shearing (σ_n: 200 kPa; v: 0.01 m/s; δ_s: 100 m)	3	Mitchell and Soga (2005); Zhang et al. (2020)	Accelerating voltage:3 kV; secondary electrons; magnification = 50×, 500×, 1000×, 2000×
X-CT test	Quartz sand	Local scans during shear displacements of 0.1, 1, 10, and 100 m (σ_n: 200 kPa; v: 0.01 m/s)	4	Gao et al. (2024)	Scanning voltage: 130 kV, current: 120 μA, resolution: 26 μm, pixel volume: 26 μm; number of slices: 1100-1300
Particle analysis test	Quartz sand	Particle size analysis in the actual shear zone at during shear displacements of 0.1, 1, 10, and 100 m (σ_n: 200 kPa; v: 0.01 m/s)	4	ASTM D6913-04 (2009); ISO 13320 (2020)	Size overlap calibration: Sieve data (>75 μm) merged with laser data (<75 μm); Shaking duration: 15 min; Refractive index: 1.52 (particle), 1.33 (water); ultrasonic dispersion

resistance in the transient stage, respectively, and τ_{sp} and τ_{ss} are the maximum and stabilized values in the steady state stage. Fig. 4(b) shows how the sample height varies with shear distance. The ratio of shear resistance to normal stress is defined as the friction coefficient μ, and Fig. 4(c) shows how it evolves with displacement.

For the samples under low normal stress (σ_{n} = 50 kPa), the friction coefficient μ_{sp} in the steady state stage declined gradually after reaching the maximum, stabilizing at 0.91 near a shear displacement of 30 m. Initially, the samples exhibited shear dilatation, but at large displacements (δ_{s} = 2 m), particle fragmentation led to a gradual reduction in dilatancy. In contrast, under high normal stress (σ_{n} = 400 kPa), a pronounced post-peak reduction in friction occurred, with the final μ stabilizing at 0.64. High normal stress effectively suppressed shear-induced dilation, causing continuous compression during steady shear (Dong et al., 2021). Variations in height change across samples reflect differing degrees of particle fragmentation under varying σ_{n} (Fukuoka et al., 2007). Notably, Hu et al. (2022a) observed that quartz sand under high pressure (1 MPa) and shear velocity (1 m/s) exhibited

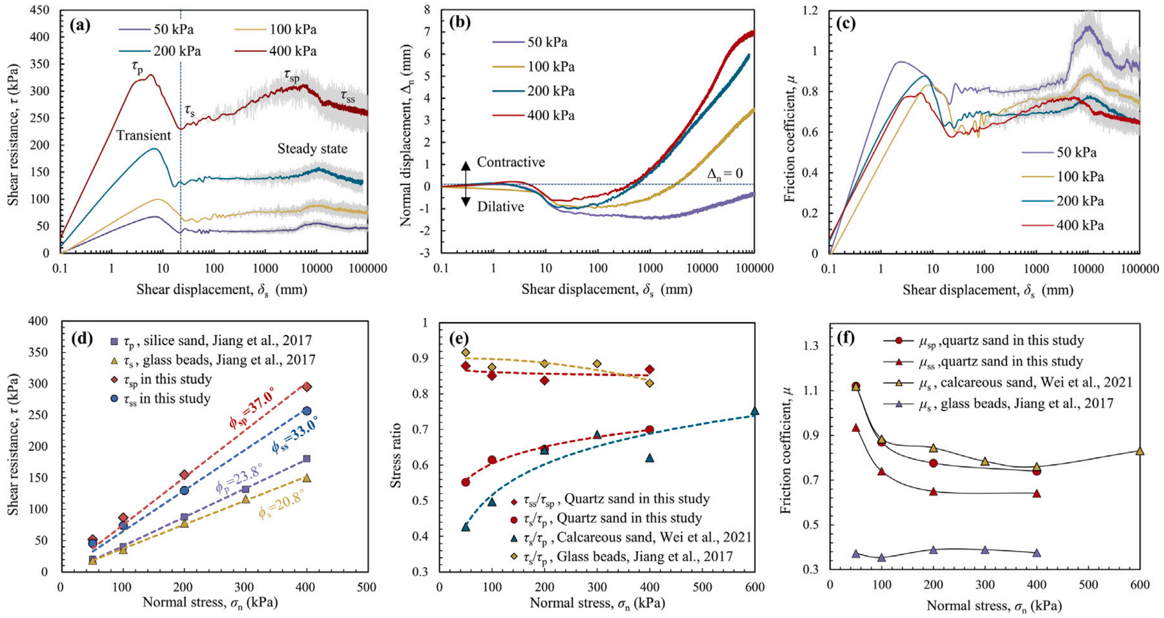

Fig. 4. Shear behavior of quartz sand under different normal stresses: variation of (a) shear resistance τ, (b) normal displacement Δ_n, and (c) friction coefficient μ against shear displacement δ_s; (d) strength envelopes; (e) stress ratio, and (f) friction coefficient μ against normal stress σ_n. The shear velocity is 0.01 m/s, and the shear displacement is 100 m.

localized transitions from shrinkage to dilation in thickness, attributed to particle embedding and filling effects (Chang and Deng, 2017). However, this transition was localized and prolonged shearing ultimately led to overall contraction, consistent with this and prior studies.

Furthermore, from the test results, the characteristic values of the apparent friction angle ϕ, shear ratio τ_{ss}/τ_{sp}, and friction coefficient μ under transient and steady state conditions were calculated, as shown in Fig. 4(d)–(f). The apparent friction angle, defined by Sassa et al. (2014) as $\tan^{-1}(\tau/\sigma)$, is a critical parameter for assessing landslide mobility. In this study, the peak friction angle ϕ_{sp} and steady state internal friction angle ϕ_{ss} of quartz sand were determined to be 37.0° and 33.0°, respectively, having higher strength than spherical granular materials such as glass microspheres. The strength ratio, which reflects the extent of shear strength degradation from peak to steady state residual shear stress, is illustrated in Fig. 4(e). The results indicate that the stress ratio (τ_s/τ_p and τ_{ss}/τ_{sp}) increases or remain relatively stable with normal stress, suggesting that higher normal stress results in reduced strength decay and a diminished tendency for sample dilation. This behavior is comparable to that of crushable calcareous sand but differs significantly from non-crushable glass beads, highlighting the role of particle breakage. As shown in Fig. 4(f), elevated normal stress yields lower friction coefficients and earlier peak strength attainment. This phenomenon likely results from enhanced particle fragmentation and fine particle generation.

3.1.2. *Effect of shear rate*

Fig. 5 presents shear test results for quartz sand under constant 200 kPa normal stress at varying shear velocities (defined here as the macroscopic constant rotational velocity applied by the lower boundary). The samples demonstrate relatively limited shear-rate sensitivity under these experimental conditions. Overall, the steady state shear resistance increases with the shear velocity. When the shear velocity increases from 0.001 to 0.1 m/s, τ_{ss} rises by approximately 14%. All samples exhibit consistent compaction trends after 0.4 m displacement, with final height variations maintained within 0.81 mm. The transient stage stress ratio τ_s/τ_p decreases with shear rate, which is consistent with previous studies, while the steady-state ratio τ_s/τ_p increases [Fig. 5(c)]. Fig. 5(d) shows as the latter increases, μ_{ss} exhibits an increasing trend whereas μ_{sp} decreases and then increases.

The shear-velocity dependence of granular friction has been a key focus in geological studies, particularly in research on landslides and faults (Kang et al., 2022). Comparative analysis in Fig. 5(d) reveals that the velocity-dependent transition point varies significantly across studies, attributable to disparities in experimental conditions such as particle composition, size distribution, initial packing fraction, and loading conditions. For instance, Gou et al. (2024) reported that particle friction generally exhibits an approximately M-shaped pattern across a broad range of shear velocity, characterized by including two velocity-strengthening and two velocity-weakening regimes. This trend is not prominent in the present study, possibly due to the limited variation in shear velocity under a given normal stress. It is hypothesized that velocity dependence is closely associated with extensive particle fragmentation and the resulting microstructural changes (Hu et al., 2020), which are central to this study.

3.1.3. *Effect of shear displacement*

Four quartz sand shear tests were performed at 200 kPa normal stress and 0.01 m/s shear velocity. The tests varied only in shear displacement (0.1 m, 1 m, 10 m and 100 m) to investigate the mechanism of particle fragmentation and the evolution of particle size distribution. As shown in Fig. 6(a), the shear resistance of the sample increases slightly with the progress of shear displacement. Corresponding vertical displacements [Fig. 6(b)], demonstrate continuous particle breakage across all displacements, although the rate of normal displacement increment decreases at larger displacements. Specifically, normal displacement increases by 3.3 mm at 10 m shear displacement, but only an additional 2.63 mm (80% of the initial increment) when δ_s extends to 100 m. This nonlinear relationship indicates progressively diminishing compaction with increasing shear displacement. Furthermore, based on Fig. 6(b), the variation in the solid fraction of the sample (defined as the ratio of the actual particle volume to the total sample volume) with shear displacement was calculated. As shown in Fig. 6(d), significant particle crushing occurs predominantly during the early shearing stages, as evidenced by substantial sample shrinkage and a pronounced increase in the solid fraction. Regression analysis indicates that the solid fraction evolution follows an approximate logarithmic trend with shear distance. Similar findings have been reported by Li et al. (2024).

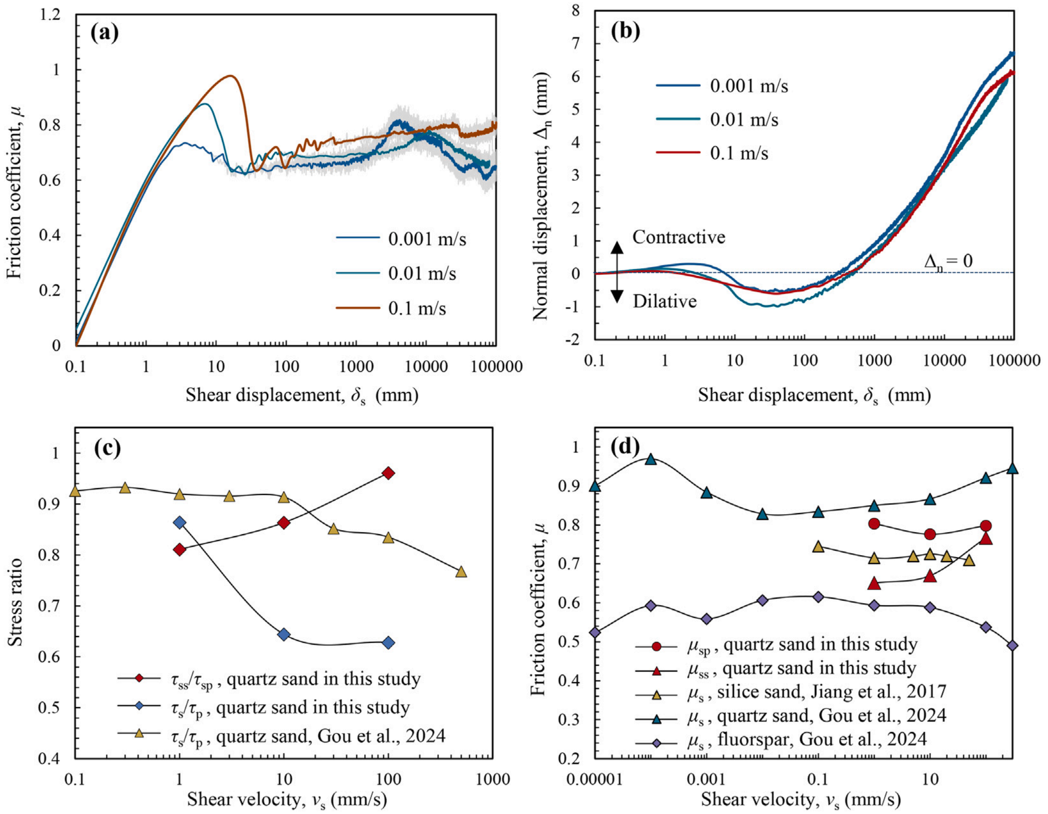

Fig. 5. Shear behavior of quartz sand under differing shear velocity: variation of (a) friction coefficient μ, and (b) normal displacement Δ_n with shear displacement δ_s; (c) stress ratio, and (d) characteristic friction coefficient μ with shear velocity v_s. The normal stress is 200 kPa, and the shear displacement is 100 m.

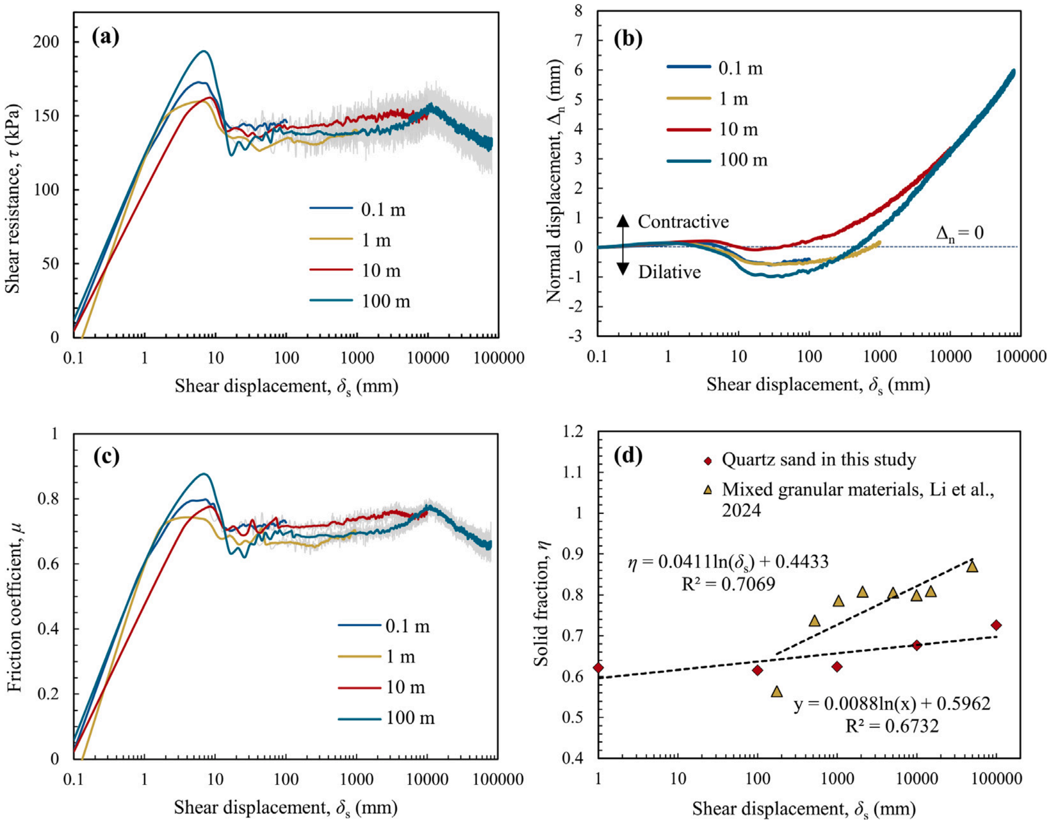

Fig. 6. Effect of shear displacement on friction behavior: variation of (a) shear resistance τ, (b) normal displacement Δ_n, (c) friction coefficient μ, and (d) solid fraction η with shear displacement δ_s. The normal stress is 200 kPa, and the shear velocity is 0.01 m/s.

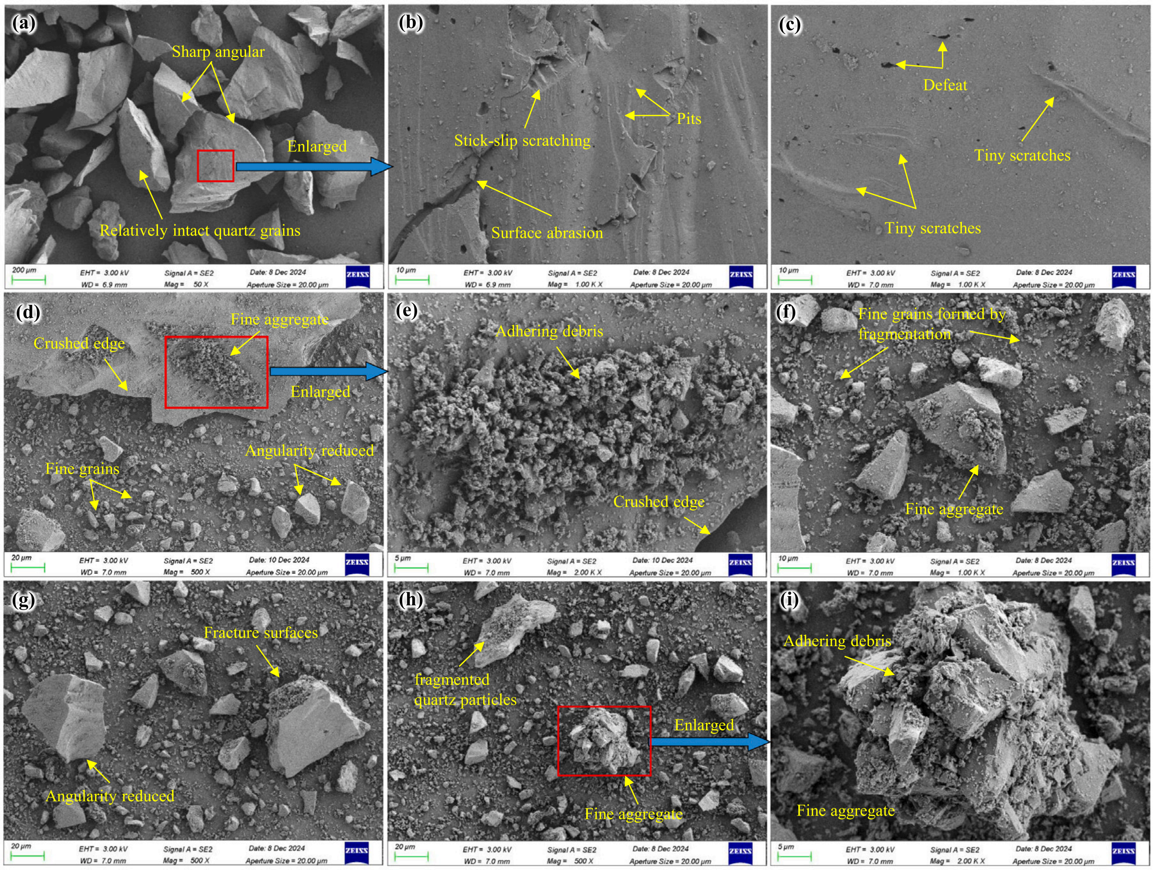

Fig. 7. Microscopic evidence of particle fragmentation: (a) crushed quartz particles after sieving; (b) surface abrasion and residual scratches caused by particle interaction; (c) defects on surface of quartz debris; (d) adhesion of debris on surface of larger particles; (e) magnified view of adhered debris; (f) crushed fine-grained quartz; (g) cross-section of fractured particles; (h) fine-grained aggregate; (i) magnified view of (h).

3.2. *Dynamic evolution of particle fragmentation*

3.2.1. *Microscopic observation*

SEM analysis of sheared quartz sand reveals fragmentation patterns and interparticle interactions. Fig. 7(a) shows larger particles (approximately 0.25–0.5 mm) sieved from the sheared sample. To enhance the visibility of morphological features such as sharp edges and surface textures, most fine particles were washed away. Local magnification in Fig. 7(b) and (c) reveal varying degrees of wear and fracture marks, with clear scratches indicating sliding interactions between particles under high normal stress. Additionally, the presence of small pits resembling impact craters [Fig. 7(b)] hints that the granular flow may behave akin to a gas-like medium under high-speed shearing, where inter-particle interactions become predominantly collision-driven (Gou et al., 2024). The SEM analysis of smaller-sized quartz sand fragments provides further insights into the fragmentation process. Fig. 7(d) clearly shows the fractured edges of larger quartz particles, demonstrating how extensive breakage leads to the generation of numerous small debris particles. Small debris adhering to larger particle surfaces, as shown in Fig. 7(e), may influence the friction coefficient of the granular assembly. The presence of fine debris could have a lubricating effect, altering the mechanical response of the sample. Fig. 7(f) demonstrates that the angularity of the crushed particles is reduced, while the adhered debris increases surface roughness. This adhesion and filling of fine particles reduces porosity and promotes sample compaction, explaining the observed height changes during shearing.

In Fig. 7(g), a clear cross-section of a fractured quartz particle is observed. The fracture process roughens the particle surface, with fracture steps and irregular features. Debris adhering to the fracture surfaces may contribute to an uneven particle texture, potentially affecting particle flow stability. Agglomerates composed of quartz debris are also observed in Fig. 7(h) and (i). This small debris gathers or adheres to the surface of slightly larger particles, forming a wrapping or covering effect. This adhesion behavior may be facilitated by weak interparticle forces (e.g., electrostatic or van der Waals forces) generated during the shearing of dry particles (Hu et al., 2015). Such adhesion reduces the effective contact between large grains and reduces friction. Additionally, weak connections between fine debris and larger particles may create a more fragile overall structure. This distinctive microstructural evolution explains the dynamic decrease in shear resistance observed after the peak residual strength during shearing [as shown in Fig. 4(a)]. Simultaneously, the continuous process of particle fragmentation increases the population of fine grains that can directly interact with larger particles. The inclusion and lubrication effects of fine grains inhibit further fragmentation of large grains (Hu et al., 2022a), creating a self-limiting mechanism that accounts for the persistence of larger particles within the shear zone even after extensive shearing displacement.

3.2.2. *Particle fragmentation microscopic visualization*

To elucidate the particle-scale mechanisms underlying the macroscopic shear behavior, X-ray CT scans were performed systematically to capture the microstructural evolution at progressive shear displacements (0.1, 1, 10, and 100 m). The initial grayscale images were adjusted for brightness and contrast to enhance the microstructural details, then a 3D visualization model was constructed based on the grayscale slices (Fig. 8). Initial fragmentation became detectable at 0.1 m displacement, manifested as localized grain size reduction near

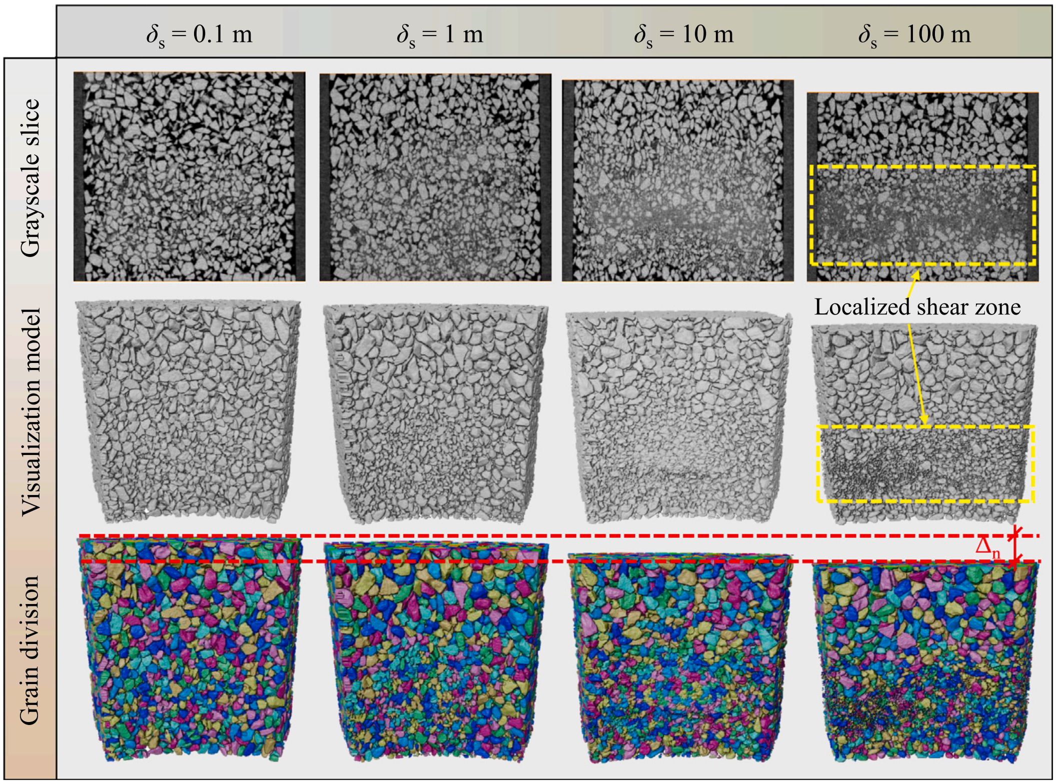

Fig. 8. Grayscale slice and visualization model of a representative quartz sand sample.

the shear plane while preserving angular coarse grains and open voids in upper/lower regions. Progressive shearing to 1 m displacement intensified the particle breakage near the shear plane, generating fine particles that accumulated in localized zones, creating heterogeneous density distributions. The filling of fine grains led to local densification, while most voids became concentrated in the upper shear zone because of shear-induced fragmentation and gravitational effects. The 10 m displacement stage exhibited comprehensive microstructural reorganization, characterized by abundant fine particles enveloping larger grains and forming polycrystalline clusters that replaced direct coarse grain contacts. These tomographic observations demonstrate excellent correlation with SEM evidence of grain boundary fractures and surface wear patterns. This slip displacement corresponds to the steady state shear maximum phase, where multiple discontinuous slip bands were observed in cross-sections. Under a normal stress of 200 kPa, frictional weakening initiated at approximately 10 m of displacement and then progressively stabilized (Fig. 6). As the δ_s approached the final 100 m (Fig. 8), the granular structure showed limited further structural change, indicating it had essentially stabilized into a steady state configuration. During this stage, particle fragmentation and redistribution asymptotically approached a limiting condition, with localized shear interfaces emerging as relatively continuous particle bands. The development of shear interfaces signifies that particle friction had achieved maximal weakening and stabilized in the steady state (Chang et al., 2024). Additionally, within the central shear zone, certain large grains remained intact, while those situated farther from the shear plane were significantly coarser than proximal grains, indicative of a graduated size distribution shaped by shear-induced sorting mechanisms.

4. Discussion

4.1. Determination of shear zone

As evidenced in Fig. 8, the shear zone remains finite despite progressive slip, consistent with prior studies (Fukuoka et al., 2007; Qannadizadeh et al., 2022). Accurate quantification of this zone is essential because particle breakage potential must be evaluated within the localized shearing region rather than the entire sample, particularly in experiments with variable filling heights. In previous studies, significant discrepancies in PSD-based crushing potential have arisen because of methodological variations, including instrumentation differences, sample height inconsistencies, and divergent shear zone determination approaches. For instance, some studies have analyzed only grains smaller than the initial particle size, assuming that only fragmented particles contribute to grain size distribution, while overlooking the presence of larger grains at the shear interface. Conversely, studies that base grain size analysis on the entire sample were undoubtedly influenced by sample height and instrument limitations (Jiang et al., 2017; Li et al., 2024), potentially underestimating the extent of particle fragmentation. To overcome these limitations, an integrated approach combining X-ray tomography with ring shear tests was developed in this study to assess the shear zone effectively, thereby enabling refined analysis of particle breakage potential. During long-distance shear, shear forces at the shear interface induce particle breakage, generating fine particles that progressively occupy intergranular voids. This process leads to densification, reduced porosity, and an increase in solid fraction. Although a minor thickness error caused by prolonged shear diffusion within the confined shear box cannot be entirely eliminated, the layer-by-layer distribution of local solid fraction remains a potentially viable indicator for characterizing the steady-state shear-affected zone, with its spatial variation providing a quantitative basis for defining the shear zone boundaries. Based on CT scan results, the solid fraction distribution along the sample height was calculated, as shown in Fig. 9.

As the shear progresses, the initially uniform distribution of solid fraction η_i becomes increasingly heterogeneous. The dashed line in Fig. 9 represents the sample-wide average solid fraction, which aligns closely with the results in Fig. 6(d). The minimal and negligible errors are attributed to the CT scan precision and compositional segmentation. At a shear displacement of 0.1 m, a slight increase in the solid fraction near the shear zone was recorded, with the maximum solid fraction

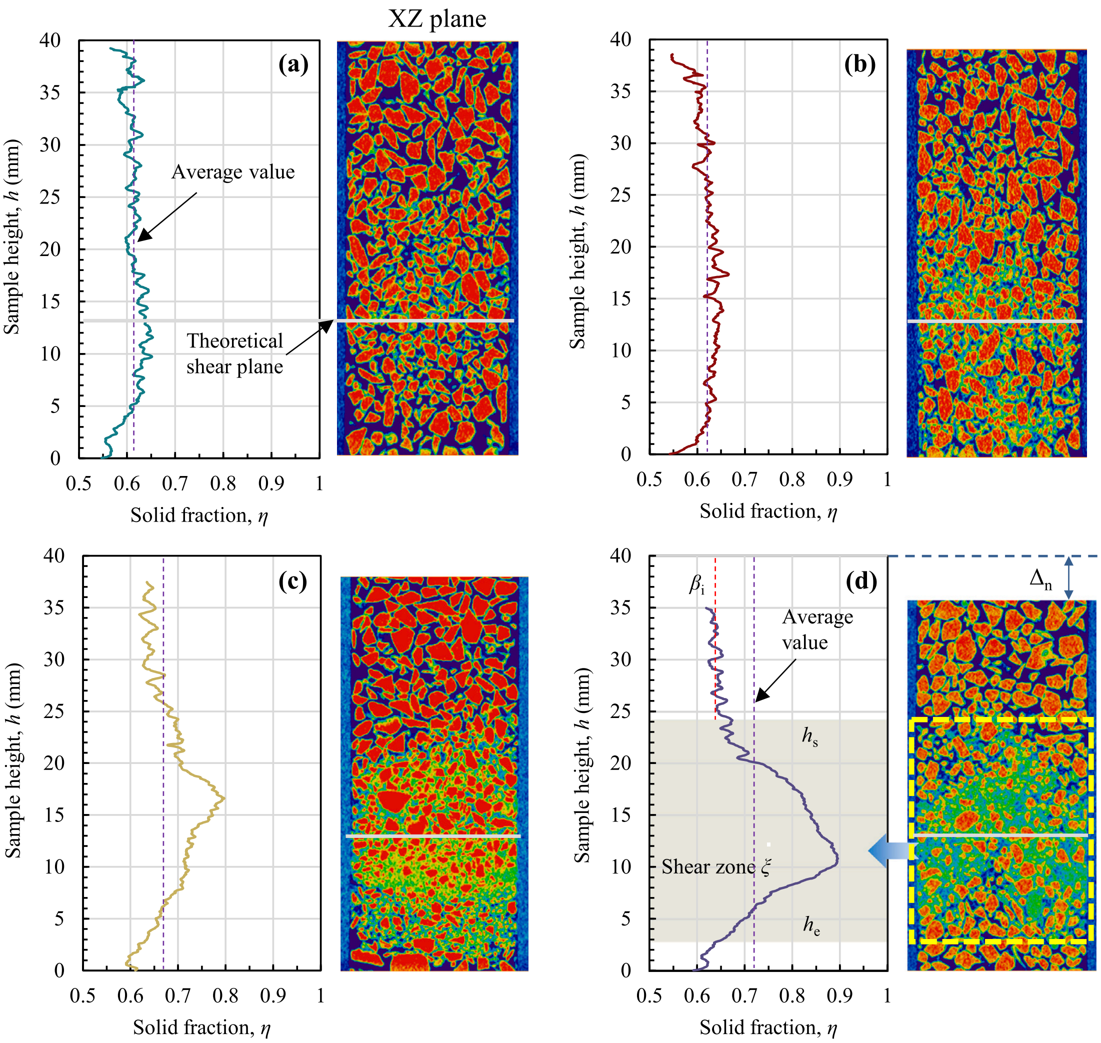

Fig. 9. Variation of solid fraction along sample height: shear displacement of (a) 0.1 m, (b) 1 m, (c) 10 m, and (d) 100 m. The h_s and h_e are the upper and lower boundary heights of the shear-affected zone, respectively.

exceeding the average by 5.8%, further confirming that particle fragmentation initiates at small shear displacements. When δ_s = 10 m, a pronounced axial peak in the solid fraction emerged along the axial direction of the sample, with the maximum solid fraction reaching approximately 0.80, a 15% increase compared to the average. Following further shear to 100 m, a distinct shear interface developed, and the maximum solid fraction increased to 0.89. The fine particles generated via fragmentation effectively filled the surrounding voids, altering the sample structure. These findings support redefining the steady-state shear-affected zone thickness (ξ) through layer-wise solid fraction variations. Specifically, the shear-affected zone and undeformed zone can be delineated by comparing the deviation of the solid fraction from the dynamic statistical baseline across successive layers. The solid fraction fluctuation threshold ($\Delta\eta$) is established based on the critical condition of material microstructure evolution. When the local solid fraction deviates from the baseline beyond this threshold, it signifies the onset of plastic deformation. This approach quantitatively correlates shear-affected zone with micromechanical response, eliminating the subjectivity inherent in traditional empirical criteria. The actual shear-affected zone thickness is defined as:

$$\xi = h_s - h_e \tag{1}$$

where h_s denotes the initial upper boundary height of the shear-affected zone from the sample top, and h_e represents its lower boundary.

The boundaries are determined by computing the average solid fraction of the first k layers as the shear-unaffected statistical baseline, i.e., $\beta_k = \frac{1}{k}\sum_{i=1}^{k}\eta_i$. A relative deviation threshold ($\Delta\eta$ = 5%) is set as the critical value for significant particle fragmentation. This value was determined based on the average fluctuation observed in a typical unfractured impact zone. To verify its reliability, a sensitivity analysis using thresholds from 3% to 7% was conducted (seeing Fig. S3 of Supplementary Material). While absolute thickness values vary slightly with the threshold, the overall evolutionary trend remains highly consistent. The 5% threshold was ultimately selected because it optimally captures the boundaries and best aligns with direct visual observations from our preliminary tests using a transparent shear cell. Notably, this threshold may be influenced by factors such as mineral properties, material morphology, and bulk density. Nevertheless, it provides a unified, objective criterion to evaluate shear zone evolution for a given material, significantly reducing subjective human error. Statistical validation of this threshold across different materials represents an intriguing avenue for future research. A layer is classified within the shear-affected zone if its solid fraction satisfies $\frac{|\eta_{i+1}-\beta_i|}{\beta_i} \geq 0.05$, with the last threshold-exceeding positions recorded as h_s and h_e, respectively.

$$h_s = \left\{ h_{i+1} \,\middle|\, \frac{|\eta_{i+1}-\beta_k|}{\beta_k} \geq 0.05 \right\} \tag{2}$$

$$h_e = \left\{ h_{j+1} \,\middle|\, \eta_{j+1} \leq \beta_k \right\} \tag{3}$$

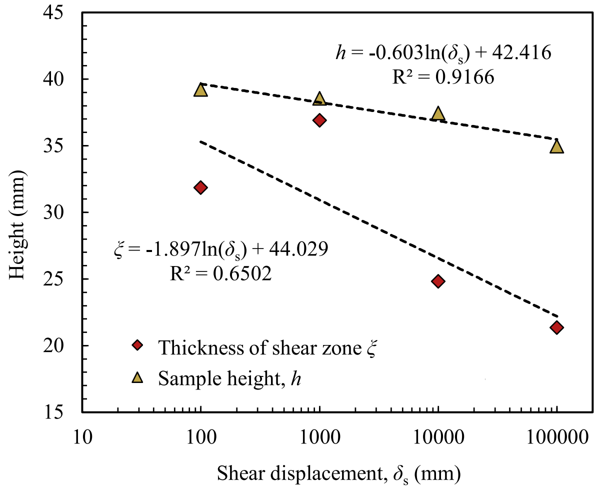

Fig. 10. Dynamic evolution of shear zone thickness ξ.

where the layer-by-layer solid fraction η_i is quantified via voxel count (particle-phase voxels/total voxels), while β_k represents the sliding reference homogeneity, characterizing the statistical baseline.

As illustrated in Fig. 9(d), the actual shear zone is distinctly demarcated, beyond which particle fragmentation is negligible. The computational results exhibit strong agreement with the right rendered XZ slice image (Fig. S2 of Supplementary Material). This method yields a final shear zone of approximately 9 to 18 times the d_{50}. This calculated range is highly consistent with the 10–20 d_{50} range observed in classical geotechnical experiments (Tatsuoka et al., 1990; Sadrekarimi and Olson, 2010; Vangla and Latha, 2015), thereby validating the method's efficacy. Fig. 10 illustrates the calculated height variation of quartz sand particle material and the evolution of shear-affected zone during shear deformation. As δ_s increases, the sample height decreases progressively, reflecting material densification. This process exhibits an approximately linear relationship with the logarithm of δ_s. The reduction in ξ signifies the localization trend of shear deformation into a confined zone, driven by energy redistribution resulting from particle crushing, directional rearrangement, or internal frictional dissipation within the shear zone. At higher δ_s, the shear zone may reach a dynamic equilibrium state, with its thickness stabilizing, indicating microstructural reorganization and the establishment of steady state shear flow. Consequently, it should be emphasized that this threshold-based identification method is more reliable during the steady-state shear phase, where the shear-affected zone is fully developed and structurally stable.

4.2. *Localized fragmentation quantification*

Shear deformation and particle fragmentation demonstrate distinct localization characteristics in ring shear tests, differing fundamentally from the global fragmentation mechanisms observed in conventional triaxial or compression tests. The strain concentration within narrow shear-affected zone renders conventional bulk particle analysis methods inadequate, as unbroken particles outside shear zone introduce a dilution effect that obscures the true fragmentation evolution patterns. This limitation systematically biases fragmentation assessments in ring shear testing and impedes understanding of microstructural changes within shear zone and their correlation with macroscopic mechanical responses. To address this, this study innovatively combined CT 3D reconstruction with quantitative shear-affected zone measurement, using spatial localization to eliminate interference from intact particles. This approach overcomes the limitations of conventional bulk analysis while providing crucial experimental evidence for understanding spatiotemporal fragmentation evolution and its role in shear strength degradation.

Using calculated actual shear-affected zone thickness, the quantification and exclusion of all particles outside this zone were performed through equivalent calculations in subsequent analyses. Specifically, the volume of the unsheared region was determined. Given the uniform initial grain size and identical mineral density of the quartz sand, this volume was converted into an equivalent mass of intact particles, which was then subtracted from the coarse fraction of the bulk PSD. This methodology effectively minimizes sample size and instrument effects, revealing intrinsic material fragmentation behavior. Fig. 11(a) presents modified PSD results for quartz sand during progressive shear displacement. Increasing displacement shifts the PSD curves toward the upper left, indicating growing fine particle content and reduced coarse fractions, particularly for particles of 1 mm and greater in diameter. d_{50} steadily declines from 1.3 mm initially to 0.37 mm after 100 m of shear displacement within the actual shear zone.

The relative breakage rate B_r, proposed by Hardin (1985), was introduced to quantify granular material fragmentation, i.e.,

$$B_r = B_t / B_p \tag{4}$$

where B_t is the actual total breakage ratio, quantified as the shaded area between initial and final PSD curves and the line of d = 0.075 mm; meanwhile, B_p denotes the potential breakage, corresponding to the area between the initial PSD curve and d = 0.075 mm, as illustrated in Fig. 11(c).

Fig. 11(d) presents the variation of B_r with δ_s, along with comparative data for calcareous sands from previous studies (Coop et al., 2004). As can be seen, B_r increases logarithmically with δ_s, consistent with previous findings (Wang and Huang, 2023) despite experimental variations. Quartz sand exhibits minimal initial breakage (B_r = 0.18 at 0.1 m displacement), followed by rapid increase to B_r = 0.58 at 10 m displacement, reflecting intense fragmentation. Beyond this point, the growth rate in B_r diminishes due to shear interface formation and structural stabilization through frictional reorganization. To theoretically validate the subsequent diminishment in the breakage growth rate, the effective selection function was evaluated based on comminution theory (Artoni et al., 2017). As detailed in Fig. 11(b), the calculated selection function decreases continuously with shear displacement. This quantitatively confirms that as fine particles gradually accumulate, they form a structural matrix that buffers and protects the remaining coarse grains, thereby inhibiting further fragmentation. For calcareous sand, initial breakage occurs more rapidly, leading to earlier frictional weakening compared to quartz sand. This can be attributed to mineralogical factors, as calcareous sand consists of calcium carbonate-based grains, which generally exhibit lower angularity and higher friability than quartz sand. These characteristics promote a more abrupt and homogeneous fragmentation pattern under shear, whereas quartz sand, with its higher angularity, tends to experience more prolonged grain interlocking and gradual fragmentation. Furthermore, differences in particle shape may also contribute to variations in shear zone dynamics. Quartz particles, due to their greater hardness and angularity, tend to break into smaller, more angular fragments and may exhibit a more gradual frictional weakening.

4.3. *Evolution of particle morphology*

Recent advancements in particle characterization have shifted from conventional 2D analysis (size and content) to 3D analysis incorporating size, morphology, and content. This transition enables more comprehensive characterization of particulate systems. Herein, this study used visualization models that captures not only size and content variations from particle fragmentation but also morphological evolution through wear and abrasion processes. Research has shown that particle morphology significantly influences microstructure formation in dense granular flows (Hu et al., 2023; Shi et al., 2024). A key

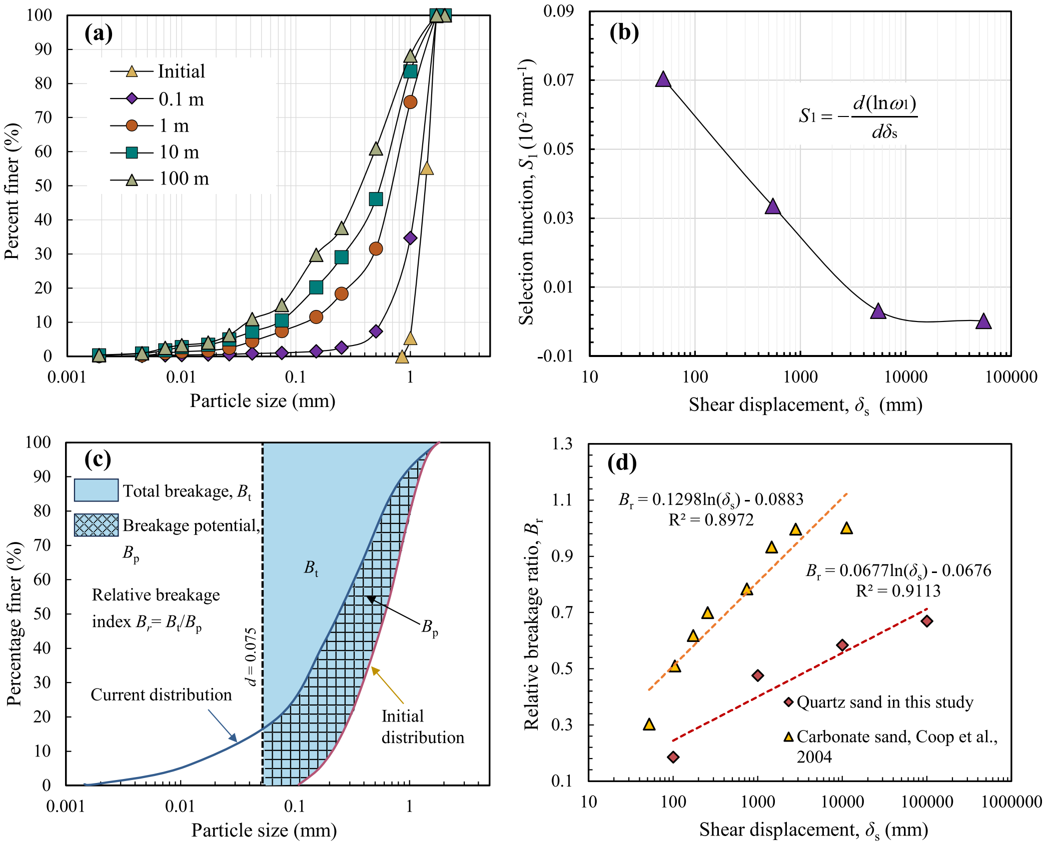

Fig. 11. Particle fragmentation characteristics for quartz sand upon shear loading: (a) variations in PSD of quartz sand with δ_s; (b) estimate of the selection function S_1 versus δ_s, where ω_1 is the surviving mass fraction of the initial coarse particles; (c) definition of relative breakage ratio; (d) variations in B_r of quartz sand with δ_s.

morphological parameter is the sphericity ψ, defined as the degree to which a particle's shape approximates that of a sphere (Sezer et al., 2008). Following the isoperimetric inequality, ψ ranges from 0 to 1, where $\psi = 1$ represents an ideal sphere. Both particle size distribution and sphericity fundamentally govern granular packing properties, including compaction behavior, density, and rheological characteristics. The classical definition by Wadell (1932) expresses sphericity as:

$$\Psi = \frac{S_n}{S} = \frac{(36\pi V^2)^{\frac{1}{3}}}{S} \tag{5}$$

where S is the actual surface area of the particle, S_n denotes the surface area of a volume-equivalent sphere, and V is to the particle volume.

Because of imaging discretization, the estimation accuracy of surface area decreases with fewer representing voxels. To avoid CT resolution limits and the effect fine particle agglomeration, sphericity was analyzed statistically only for particles with an equivalent diameter greater than 0.25 mm. Fig. 12 reveals a gradual increase in overall sample sphericity with progressive shearing. Fine particles generated via fragmentation exhibit higher average sphericity compared to the parent particles; for instance, when $\delta_s = 100$ m, the average sphericity of particles in the range of 0.25–0.5 mm reaches 0.842, an increase of 0.105 relative to the parent particles. This phenomenon reveals a coupled mechanism between particle fragmentation and morphological evolution: first, stress concentrations promote preferential fracture along internal weak planes, producing fragments with geometries that approximate the equiaxed cleavage surfaces of the parent particles, thereby having a higher initial sphericity; second, because of the increased specific surface area, fine particles are more likely to undergo rolling-dominated motion during continuous shearing, with their edges experiencing to more frequent friction and abrasion, which accelerates the mechanical exfoliation of surface micro-projections. This rounding process is driven more by interactions among particles of varying sizes. Mirghasemi et al. (2002) and Cho et al. (2006) have confirmed that the reduction in particle angularity and roughness promotes lower shear strength and influences the evolution of stress-induced anisotropy. Consequently, during the shear of quartz sand, the increase in average sphericity further reduces interlocking at particle contact surfaces, potentially leading to lower peak and steady state shear strengths as well as reduced dilation. The above results show that not only does particle crushing reshape the material gradation through fine granulation but also its accompanying rounding effect significantly affects the macroscopic mechanical response by reducing the bite between particles.

4.4. Microscopic mechanism

To elucidate the mechanical principles governing granular shear behavior, comparative experiments were conducted using halite and glass beads under identical loading conditions. The halite exhibited significantly higher fragmentation propensity than quartz sand, while the glass beads maintained negligible morphological and dimensional alterations after shearing. The experimental results for both materials are presented in Fig. 13. Similar to quartz sand, the halite displayed three characteristic frictional phases: initial transient response, friction strengthening, and strain softening to steady state. This triphasic behavior aligns with observations in crushable geomaterials (Hu et al., 2022b; Chang et al., 2024). Additionally, higher normal stresses led to a more pronounced post-peak stress drop and a smaller shear displacement at peak stress, consistent with the quartz sand results in Fig. 4. Notably, the halite demonstrated unexpectedly limited normal displacement under high stress, which may be related to shear localization and the formation and extension of a well-defined shear plane (Chang

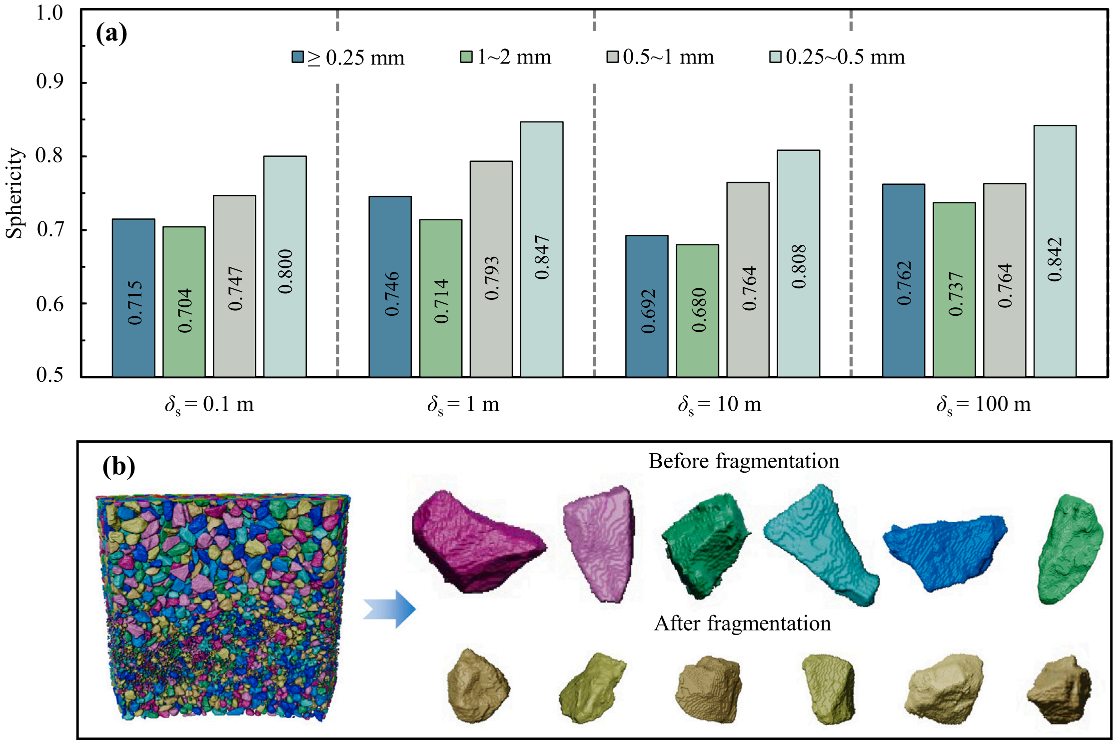

Fig. 12. Evolution of particle morphology: (a) sphericity variation with δ_s for entire particle group and individual size range; (b) several typical particle morphologies extracted from 3D visualization model, with the upper side showing the unbroken initial particles (high angularity) and the lower side showing the fine particles after shear crushing (relative high roundness).

et al., 2024). Conversely, the shear resistance of non-fragmenting glass beads remained relatively stable throughout the steady state shearing process, with minimal volume changes; this is attributable to their spherical geometry enabling strain accommodation through particle rolling, a low-energy deformation mechanism that minimizes frictional resistance and maintains volumetric stability. These comparative experiments indicate that shear-induced fragmentation and spheroidization is the primary driver of the observed frictional transitions in crushable granular materials. Notably, quantitative PSD and B_r analyses focused solely on quartz sand. For glass beads and halite, post-shear sieving analysis was practically unfeasible due to the negligible crushing ratio of glass beads (< 1%) and the rapid agglomeration and hardening of hygroscopic halite fines into crust-like aggregates.

The behavior of natural landslide materials is highly complex, as variations in discrete particle properties, sizes, and shapes significantly influence shear patterns and interactions, thereby affecting the evolution of frictional strength and instability. Although the idealized end-member materials used herein (quartz sand, halite, and glass beads) do not fully replicate the mineralogical heterogeneity and broad gradation of actual landslide deposits, they effectively isolate the mechanical role of crushability. Consequently, while the specific threshold displacements and absolute strength drops will inevitably vary for field-relevant materials containing clays or multi-mineral aggregates, the underlying dynamic transition from interlocking to comminution-driven fluidization remains fundamentally applicable. In crushable materials, the dynamic decrease in shear resistance is considered to be directly related to the initiation and movement of landslides (Dieterich, 1978; Jiang et al., 2016). Based on the present analytical results, this study proposes a synergistic fragmentation–spheronization mechanism for crushable materials, providing a comprehensive explanation for the evolution of frictional behavior and microstructural changes. During long-distance shearing, the granular friction behavior exhibits a distinct three-stage evolution characterized by two shear resistance peaks (Fig. 14), driven by the dynamic coupling of particle fragmentation, morphological evolution, and structural reorganization. These evolutionary stages are demarcated by the critical peak states of the macroscopic friction coefficient, which directly mirror the underlying microstructural shifts. Note that here, L_t, L_s, and L_w are the characteristic slip lengths of these three phases, respectively (refer to Chang et al. (2024)). L_t is likely associated with the characteristic length over which initial force chains percolate or propagate through the granular material, reflecting the spatial extent of the force transmission network within the granular material; L_s represent the critical fragmentation thickness, marking the point at which fragmentation dominates the shear response, while L_w could be interpreted as the characteristic width of the shear zone, indicating the extent of plastic deformation during shear.

The friction coefficient (μ) initially rises rapidly during the transient stage, reflecting the mobilization of interparticle contacts and the formation of force chains (Jiang et al., 2016), until a local peak strength (μ_p) is reached at a displacement $\delta_s = L_t$. This initial peak corresponds to a metastable configuration of the granular skeleton, with minimal particle fragmentation and localized deformation (Stage I).

Following this, the system enters a strengthening stage, during which μ gradually increases toward a second, more stable peak value (μ_{sp}). This stage is driven by progressive compaction, interlocking of angular particles, and enhanced force chain stability. Moderate fragmentation begins to occur, producing angular fragments that contribute to increased interparticle friction and dilation (Stages II–III). The displacement at which this peak occurs is denoted $\delta_s = L_s$, beyond which the shear resistance begins to decline.

The weakening process dominates the final stage, marked by a pronounced drop in μ beyond the peak (μ_{sp}), eventually stabilizing at a residual strength (μ_{ss}). This post-peak reduction in shear resistance arises from extensive particle fragmentation, formation of fine particles, and spheronization. The active shear zone becomes progressively thinner with accumulated strain, which is attributed to volumetric compaction and significant strain localization effects (Fukuoka et al., 2007; Chang et al., 2024). Ultimately, this leads to the development of a localized, low-friction shear zone filled with rounded fragments

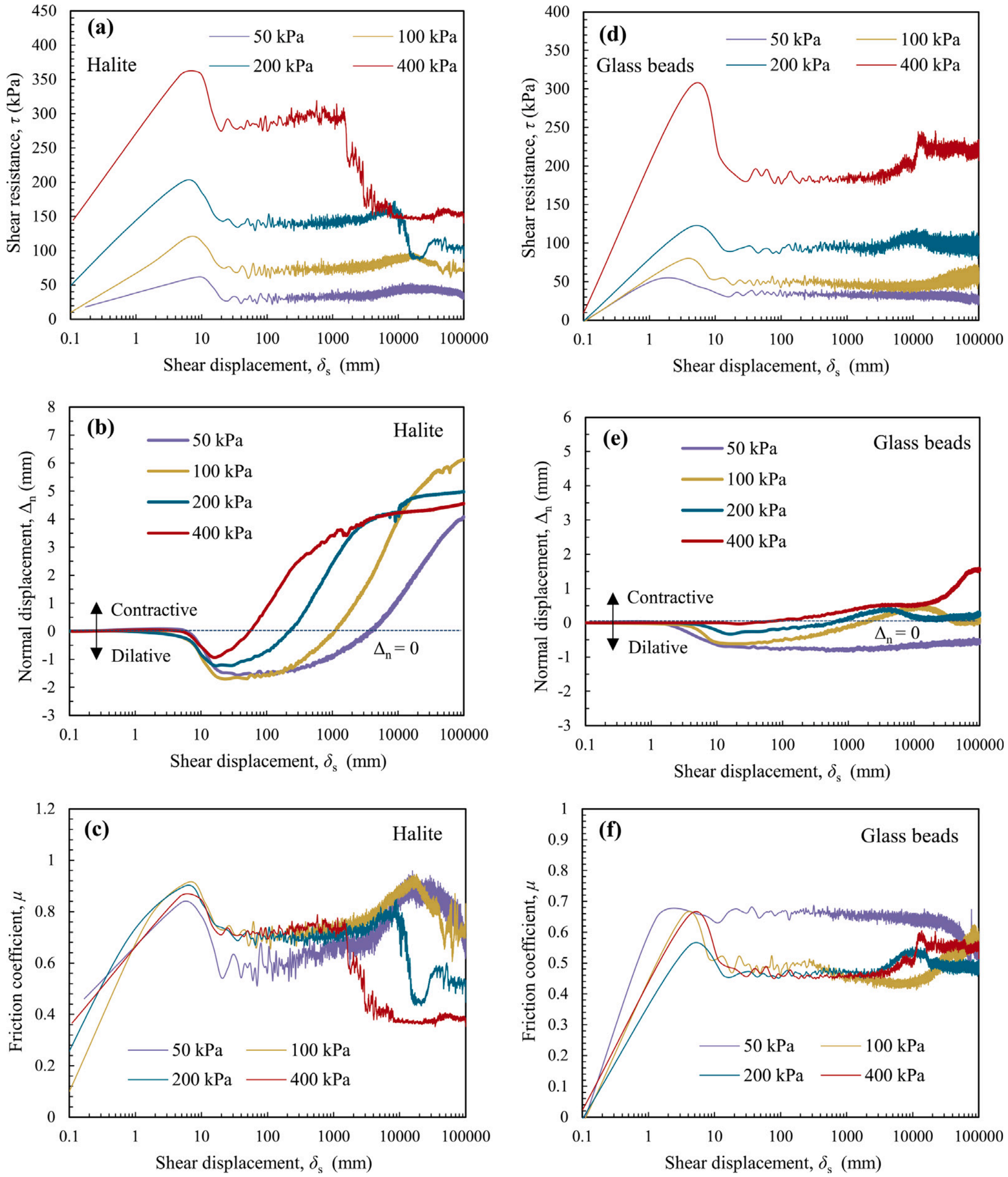

Fig. 13. Shear behavior of glass beads under different σ_n: variation of (a) shear resistance τ, (b) normal displacement Δ_n, and (c) friction coefficient μ against the shear displacement δ_s; shear behavior of halite under different σ_n: variation of (d) shear resistance τ, (e) normal displacement Δ_n, and (f) friction coefficient μ against the shear displacement δ_s. The shear velocity is 0.01 m/s, and the shear displacement is 100 m.

(Stage IV). These fine particles act as lubricants, promoting particle rolling and suppressing interlocking, thus facilitating sustained shear at low resistance (Reches and Lockner, 2010; Chen et al., 2013).

This triphasic behavior underscores a synergistic interplay among particle crushing, morphological evolution, and strain localization. These observations provide a structural complement to the widely adopted $\mu(I)$ rheology (Jop et al., 2006). The dynamic frictional weakening is a synergistic outcome: shrinking particle size lowers the rheological inertial state, while increased sphericity and fines accumulation physically lubricate the shear band. Consequently, incorporating structural state variables into rate-dependent models is a possible direction for improvement. Furthermore, these structural–frictional feedbacks provide a grain-scale micromechanical basis for the theoretical model used in macroscopic avalanche modeling. Nevertheless, given the inherent kinematic disparities between confined laboratory shear and unconfined natural flows, translating these insights into field-scale mobility predictions still requires careful calibration of boundary effects and complex flow regimes.

5. Conclusions

In the study reported herein, the dynamic shear response and particle fragmentation mechanisms in granular materials under varying stress and shear conditions were investigated systematically via ring-shear tests, X-ray microtomography, and microstructural analyses. The findings provide critical insights into shear zone evolution, frictional behavior, and grain-scale processes, with implications for understanding catastrophic mass flows such as landslides and rock avalanches. The main conclusions are as follows:

(1) Higher normal stresses accelerate particle fragmentation and promote earlier steady state peak shear resistance, followed by significant frictional weakening. This weakening is attributed to fine particle enrichment within the shear zone, which reduces interparticle interlocking and facilitates lubrication.

(2) A novel method based on solid fraction fluctuations was used to delineate quantitatively the shear-affected region, revealing that

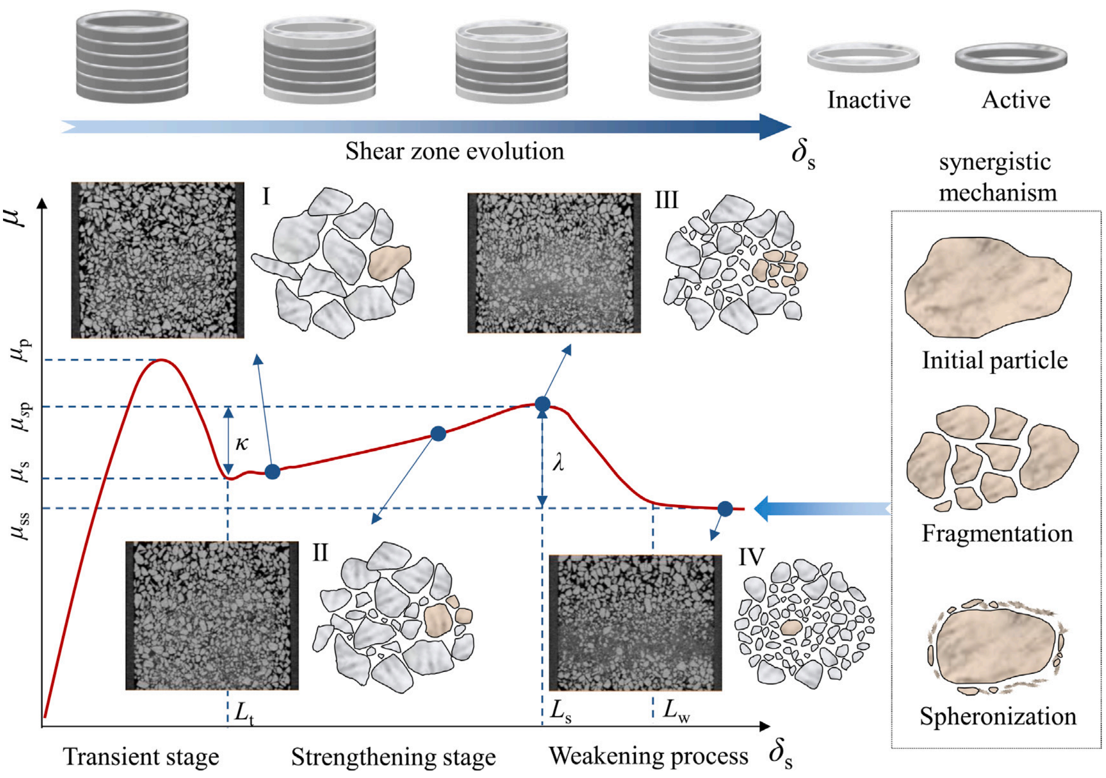

Fig. 14. Conceptual model of synergistic particle fragmentation–spheronization mechanism.

fragmentation occurs predominantly within localized bands. This quantification enables a more accurate evaluation of actual breakage ratios, and provides critical micro-macro linkages to explain shear strength degradation mechanisms in geophysical flows.

(3) Three stages of friction evolution were identified: a transient stage dominated by interparticle interlocking, a strengthening stage driven by fragmentation, and a subsequent frictional weakening stage governed by particle lubrication. The steady state shear behavior is dictated by a dynamic equilibrium between particle breakage and the rolling motion of fine grains.

(4) The proposed synergistic fragmentation–spheronization mechanism provides a comprehensive explanation to explain the mechanical behaviors of crushable materials. This mechanism highlights how particle crushing degree, localized shear zone thinning and particle sphericity collectively control the transition from global load-bearing to localized fluidization. These findings highlight the critical influence of particle fragmentation on shear dynamics, with implications for modeling geophysical flows such as landslides and fault zone evolution under high-stress regimes.

It is worth noting that only dry particulate materials with a single initial particle size distribution were considered in this study. While such idealized reference materials are crucial for strictly isolating the fundamental mechanisms of fragmentation, future testing involving complex natural geomaterials is inevitably required to calibrate these findings for site applications. However, this manuscript represents the preliminary phase of our ongoing research. A clear understanding of the dominant roles of friction evolution and particle fragmentation–spheronization is essential before further investigating key factors such as pore water pressure, polydisperse systems, and field validation.

CRediT authorship contribution statement

Haodong Gao: Writing – original draft, Visualization, Investigation, Formal analysis, Conceptualization. **Shun Wang:** Writing – review & editing, Validation, Methodology, Funding acquisition. **Ruijun Wang:** Writing – review & editing, Methodology, Conceptualization. **Xuan Kang:** Writing – review & editing, Methodology, Formal analysis. **Jidong Zhao:** Writing – original draft, Investigation, Data curation.

Declaration of competing interest

The authors declare that they have no known competing financial interests or personal relationships that could have appeared to influence the work reported in this paper.

Acknowledgments

This work was supported by the National Natural Science Foundation of China (Project No. 42472355).

Appendix A. Supplementary data

Supplementary material related to this article can be found online at https://doi.org/10.1016/j.enggeo.2026.108813.

Data availability

Data will be made available on request.

Particle dynamic fragmentation regulates friction and mobility in geophysical flows (Original data) (Mendeley Data)

References

Alikarami, R., Andò, E., Gkiousas-Kapnisis, M., Torabi, A., Viggiani, G., 2015. Strain localisation and grain breakage in sand under shearing at high mean stress: insights from in situ X-ray tomography. Acta Geotech. 10, 15–30. http://dx.doi.org/10.1007/s11440-014-0364-6.

Artoni, R., Cazacliu, B., Hamard, E., Cothenet, A., Parhanos, R.S., 2017. Resistance to fragmentation of recycled concrete aggregates. Mater. Struct. 50 (1), 11. http://dx.doi.org/10.1617/s11527-016-0900-y.

Baumberger, T., Caroli, C., 2006. Solid friction from stick–slip down to pinning and aging. Adv. Phys. 55 (3–4), 279–348. http://dx.doi.org/10.1080/00018730600732186.

Bian, H., Wang, S., Ma, H., Xin, P., 2024. Stability of soil-rock mixture slopes based on random field theory (in Chinese with English abstract). Bull. Geol. Sci. Tech. 43, 162–170. http://dx.doi.org/10.19509/j.cnki.dzkq.tb20240183.

Brantut, N., Schubnel, A., Rouzaud, J.N., Brunet, F., Shimamoto, T., 2008. High-velocity frictional properties of a clay-bearing fault gouge and implications for earthquake mechanics. J. Geophys. Res. Solid Earth 113 (B10), http://dx.doi.org/10.1029/2007JB005551.

Cabrera, M., Estrada, N., 2021. Is the grain size distribution a key parameter for explaining the long runout of granular avalanches? J. Geophys. Res. Solid Earth 126 (9), e2021JB022589. http://dx.doi.org/10.1029/2021JB022589.

Cai, Z., Lu, L., Huang, Q., Li, J., Zhong, L., Xiang, J., Xia, B., Liu, H., 2019. Formation conditions for nanoparticles in a fault zone and their role in fault sliding. Tectonics 38 (1), 159–175. http://dx.doi.org/10.1029/2018TC005171.

Chang, C.S., Deng, Y., 2017. A particle packing model for sand–silt mixtures with the effect of dual-skeleton. Granul. Matter 19 (4), 80. http://dx.doi.org/10.1007/s10035-017-0762-1.

Chang, C., Noda, H., Hamada, Y., Huang, C., Ma, T., Wang, G., Yamaguchi, T., 2024. Comminution-induced transient frictional behavior in sheared granular halite. Geophys. Res. Lett. 51 (21), e2024GL109645. http://dx.doi.org/10.1029/2024GL109645.

Chen, X., Madden, A.S., Bickmore, B.R., Reches, Z., 2013. Dynamic weakening by nanoscale smoothing during high-velocity fault slip. Geology 41 (7), 739–742. http://dx.doi.org/10.1130/G34169.1.

Cho, G.-C., Dodds, J., Santamarina, J.C., 2006. Particle shape effects on packing density, stiffness, and strength: natural and crushed sands. J. Geotech. Geoenviron. Eng. 132 (5), 591–602. http://dx.doi.org/10.1061/(ASCE)1090-0241(2006)132:5(591).

Collins-Craft, N.A., Stefanou, I., Sulem, J., Einav, I., 2020. A cosserat breakage mechanics model for brittle granular media. J. Mech. Phys. Solids 141, 103975. http://dx.doi.org/10.1016/j.jmps.2020.103975.

Coop, M., Sorensen, K., Bodas Freitas, T., Georgoutsos, G., 2004. Particle breakage during shearing of a carbonate sand. Géotechnique 54 (3), 157–163. http://dx.doi.org/10.1680/geot.2004.54.3.157.

Crosta, G.B., Frattini, P., Fusi, N., 2007. Fragmentation in the Val Pola rock avalanche, Italian Alps. J. Geophys. Res. Earth Surf. 112 (F1), 1–23. http://dx.doi.org/10.1029/2005JF000455.

Davies, T., McSaveney, M., 2009. The role of rock fragmentation in the motion of large landslides. Eng. Geol. 109 (1–2), 67–79. http://dx.doi.org/10.1016/j.enggeo.2008.11.004.

De Paola, N., Holdsworth, R.E., Viti, C., Collettini, C., Bullock, R., 2015. Can grain size sensitive flow lubricate faults during the initial stages of earthquake propagation? Earth Planet. Sci. Lett. 431, 48–58. http://dx.doi.org/10.1016/j.epsl.2015.09.002.

Dieterich, J.H., 1978. Time-dependent friction and the mechanics of stick-slip. Pure Appl. Geophys. 116, 790–806. http://dx.doi.org/10.1007/BF00876539.

Dong, Z., Su, L., Zhang, C., Liu, Z., Xiao, S., 2021. Transition of shear flow for granular materials in a numerical ring shear test. Granul. Matter 23, 1–9. http://dx.doi.org/10.1007/s10035-020-01062-6.

Du, C., Zhuang, J., Peng, J., Kong, J., Hu, W., 2024. Numerical investigation of the fast shear behaviour of granular materials and its significance for rapid landslides. Eng. Geol. 342, 107733. http://dx.doi.org/10.1016/j.enggeo.2024.107733.

Dunning, S.A., Armitage, P., 2010. The grain-size distribution of rock-avalanche deposits: implications for natural dam stability. In: Natural and Artificial Rockslide Dams. Springer, pp. 479–498. http://dx.doi.org/10.1007/978-3-642-04764-0_19.

Einav, I., 2007. Breakage mechanics—Part II: Modelling granular materials. J. Mech. Phys. Solids 55 (6), 1298–1320. http://dx.doi.org/10.1016/j.jmps.2006.11.004.

Fukuoka, H., Sassa, K., Wang, G., 2007. Influence of shear speed and normal stress on the shear behavior and shear zone structure of granular materials in naturally drained ring shear tests. Landslides 4, 63–74. http://dx.doi.org/10.1007/s10346-006-0053-0.

Furuki, H., Chigira, M., 2019. Structural features and the evolutionary mechanisms of the basal shear zone of a rockslide. Eng. Geol. 260, 105214. http://dx.doi.org/10.1016/j.enggeo.2019.105214.

Gao, H., An, R., Zhang, X., Wang, G., Liu, X., Xu, Y., 2024. Dynamic evolution of desiccation cracks and their relationship with the hydraulic properties of expansive soil. Int. J. Geomech. 24 (3), 04023299. http://dx.doi.org/10.1061/IJGNAI.GMENG-9299.

Gou, H., Hu, W., Xu, Q., Chen, J., McSaveney, M., Breard, E.C., Huang, R., Wang, Y., Jia, X., Zhou, L., 2024. Variation in granular frictional resistance across nine orders of magnitude in shear velocity. J. Geophys. Res. Solid Earth 129 (7), e2023JB028241. http://dx.doi.org/10.1029/2023JB028241.

Green, H., Shi, F., Bozhilov, K., Xia, G., Reches, Z., 2015. Phase transformation and nanometric flow cause extreme weakening during fault slip. Nat. Geosci. 8 (6), 484–489. http://dx.doi.org/10.1038/ngeo2436.

Hardin, B.O., 1985. Crushing of soil particles. J. Geotech. Eng. 111 (10), 1177–1192. http://dx.doi.org/10.1061/(ASCE)0733-9410(1985)111:10(1177).

Hu, W., Chang, C.S., McSaveney, M., Huang, R., Xu, Q., Zheng, Y., Yu, J., 2020. A weakening rheology of dry granular flows with extensive brittle grain damage in high-speed rotary shear experiments. Geophys. Res. Lett. 47 (11), e2020GL087763. http://dx.doi.org/10.1029/2020GL087763.

Hu, F., Xu, C., Li, H., Li, S., Yu, Z., Li, Y., He, X., 2015. Particles interaction forces and their effects on soil aggregates breakdown. Soil Till. Res. 147, 1–9. http://dx.doi.org/10.1016/j.still.2014.11.006.

Hu, W., Xu, Q., McSaveney, M., Huang, R., Wang, Y., Chang, C.S., Gou, H., Zheng, Y., 2022a. The intrinsic mobility of very dense grain flows. Earth Planet. Sci. Lett. 580, 117389. http://dx.doi.org/10.1016/j.epsl.2022.117389.

Hu, W., Xu, Q., McSaveney, M., Scaringi, G., Huang, R., Wang, G., Gou, H., Zheng, Y., 2022b. Fluid-like behavior of crushed rock flows. J. Geophys. Res. Earth Surf. 127 (10), e2021JF006523. http://dx.doi.org/10.1029/2021JF006523.

Hu, W., Zheng, Y., McSaveney, M., Xu, Q., Huang, R., Zhou, L., 2023. Evolution of the strain localization and shear-zone internal structure in the granular material: Insights from ring-shear experiments. Eng. Geol. 325, 107283. http://dx.doi.org/10.1016/j.enggeo.2023.107283.

Jiang, Y., Wang, G., Kamai, T., 2017. Fast shear behavior of granular materials in ring-shear tests and implications for rapid landslides. Acta Geotech. 12, 645–655. http://dx.doi.org/10.1007/s11440-016-0508-y.

Jiang, Y., Wang, G., Kamai, T., McSaveney, M.J., 2016. Effect of particle size and shear speed on frictional instability in sheared granular materials during large shear displacement. Eng. Geol. 210, 93–102. http://dx.doi.org/10.1016/j.enggeo.2016.06.005.

Jop, P., Forterre, Y., Pouliquen, O., 2006. A constitutive law for dense granular flows. Nature 441 (7094), 727–730. http://dx.doi.org/10.1038/nature04801.

Kang, X., Wang, S., Wu, W., Li, D., 2025. Mechanical behaviour and shear localisation of gravel soils: experimental study and numerical modelling. Géotechnique 1–22, http://dx.doi.org/10.1680/jgeot.24.01238.

Kang, X., Wang, S., Wu, W., Xu, G., 2022. Residual state rate effects of shear-zone soil regulating slow-to-fast transition of catastrophic landslides. Eng. Geol. 304, 106692. http://dx.doi.org/10.1016/j.enggeo.2022.106692.

Li, Y., Hu, W., Xu, Q., Huang, R., Chang, C., McSaveney, M., 2024. Evolution of power-law particle-size distributions in dense grain-flow experiments. J. Geophys. Res. Earth Surf. 129 (10), e2024JF007844. http://dx.doi.org/10.1029/2024JF007844.

Locat, P., Couture, R., Locat, J., Leroueil, S., 2003. Assessment of the fragmentation energy in rock avalanches. In: 3rd Canadian Conference on Geotechnique and Geohazards. 261–268. Citeseer, http://dx.doi.org/10.1139/T06-045.

Loi, D.H., Jayakody, S., Sassa, K., 2023. Teaching tool "undrained dynamic loading ring shear testing with video". In: Progress in Landslide Research and Technology 1(2):325–359. Springer, http://dx.doi.org/10.1007/978-3-031-18471-0_25.

McSaveney, M., Davies, T., 2007. Rockslides and their motion. Prog. Landslide Sci. 113–133, http://dx.doi.org/10.1007/978-3-540-70965-7_8.

Melosh, H.J., 1986. The physics of very large landslides. Acta Mech. 64 (1), 89–99. http://dx.doi.org/10.1007/BF01180100.

Mirghasemi, A., Rothenburg, L., Matyas, E., 2002. Influence of particle shape on engineering properties of assemblies of two-dimensional polygon-shaped particles. Géotechnique 52 (3), 209–217. http://dx.doi.org/10.1680/geot.2002.52.3.209.

Mitchell, J.K., Soga, K., 2005. Fundamentals of soil behavior, 3rd ed. John Wiley & Sons, New York, http://dx.doi.org/10.1002/9781119832348.

Niemeijer, A., Spiers, C., 2007. A microphysical model for strong velocity weakening in phyllosilicate-bearing fault gouges. J. Geophys. Res. Solid Earth 112 (B10), 1–12. http://dx.doi.org/10.1029/2007JB005008.

Niu, W., Zheng, H., Yuan, C., Mao, W., Huang, Y., 2024. Shear characteristics of granular materials with different friction coefficients based on ring shear test. Granul. Matter 26 (2), 26. http://dx.doi.org/10.1007/s10035-024-01398-3.

Pudasaini, S.P., Mergili, M., Lin, Q., Wang, Y., 2024. Dynamic simulation of rock-avalanche fragmentation. J. Geophys. Res. Earth Surf. 129 (9), e2024JF007689. http://dx.doi.org/10.1029/2024JF007689.

Qannadizadeh, A., Shourijeh, P.T., Lashkari, A., 2022. Laboratory investigation and constitutive modeling of the mechanical behavior of sand–GRP interfaces. Acta Geotech. 17 (10), 4253–4275. http://dx.doi.org/10.1007/s11440-022-01533-5.

Reches, Z., Lockner, D.A., 2010. Fault weakening and earthquake instability by powder lubrication. Nature 467 (7314), 452–455. http://dx.doi.org/10.1038/nature09348.

Sadrekarimi, A., Olson, S.M., 2010. Shear band formation observed in ring shear tests on sandy soils. J. Geotech. Geoenviron. Eng. 136 (2), 366–375. http://dx.doi.org/10.1061/(ASCE)GT.1943-5606.0000220.

Sassa, K., Dang, K., He, B., Takara, K., Inoue, K., Nagai, O., 2014. A new high-stress undrained ring-shear apparatus and its application to the 1792 Unzen–Mayuyama megaslide in Japan. Landslides 11, 827–842. http://dx.doi.org/10.1007/s10346-014-0501-1.

Sezer, G., Ramyar, K., Karasu, B., Göktepe, A.B., Sezer, A., 2008. Image analysis of sulfate attack on hardened cement paste. Mater. Des. 29 (1), 224–231. http://dx.doi.org/10.1016/j.matdes.2006.12.006.

Shi, K., Zhu, F., Zhao, J., 2024. Multi-scale analysis of shear behaviour of crushable granular sand under general stress conditions. Géotechnique 74 (5), 443–460. http://dx.doi.org/10.1680/jgeot.21.00412.

Tang, Y., Wang, S., Chen, L., Chen, J., Zhang, C., 2024. A gradation-density-dependent hypoplastic model for calcareous sand with particle crushing. Géotechnique 1–43, http://dx.doi.org/10.1680/jgeot.24.01284.

Tatsuoka, F., Nakamura, S., Huang, C., Tani, K., 1990. Strength anisotropy and shear band direction in plane strain tests of sand. Soils Found. 30 (1), 35–54. http://dx.doi.org/10.3208/sandf1972.30.35.

Vangla, P., Latha, G.M., 2015. Influence of particle size on the friction and interfacial shear strength of sands of similar morphology. Int. J. Geosynth. Ground Eng. 1 (1), 6. http://dx.doi.org/10.1007/s40891-014-0008-9.

Wadell, H., 1932. Volume, shape, and roundness of rock particles. J. Geol. 40 (5), 443–451. http://dx.doi.org/10.1086/623964.

Wang, D., Carmeliet, J., Zhou, W., Dorostkar, O., 2021. On the effect of grain fragmentation on frictional instabilities in faults with granular gouge. J. Geophys. Res. Solid Earth 126 (5), e2020JB020510. http://dx.doi.org/10.1029/2020JB020510.

Wang, S., Fang, H., Kang, X., Li, D., Wu, W., 2024. Simhypo-sand: a simple hypoplastic model for granular materials and SPH implementation. Acta Geotech. 19 (7), 4533–4555. http://dx.doi.org/10.1007/s11440-024-02350-8.

Wang, S., Huang, Y., 2023. Experimental study on the effect of particle breakage on the shear characteristics of large-displacement soil exposed to heat treatment. Eng. Geol. 323, 107219. http://dx.doi.org/10.1016/j.enggeo.2023.107219.

Wang, Z., Wang, G., 2022. Effect of particle breakage-induced frictional weakening on the dynamics of landslides. Granul. Matter 24 (3), 72. http://dx.doi.org/10.1007/s10035-022-01234-6.

Wang, S., Wu, W., Cui, D., 2022. On mechanical behaviour of clastic soils: numerical simulations and constitutive modelling. Géotechnique 72 (8), 706–721. http://dx.doi.org/10.1680/jgeot.20.P.184.

Wartman, J., Montgomery, D.R., Anderson, S.A., Keaton, J.R., Benoît, J., dela Chapelle, J., Gilbert, R., 2016. The 22 March 2014 Oso landslide, Washington, USA. Geomorphology 253, 275–288. http://dx.doi.org/10.1016/j.geomorph.2015.10.022.

Wei, H., Yin, M., Zhao, T., Yan, K., Shen, J., Meng, Q., Wang, X., He, J., 2021. Effect of particle breakage on the shear strength of calcareous sands. Mar. Geophys. Res. 42, 1–11. http://dx.doi.org/10.1007/s11001-021-09440-2.

Zhang, X., Liu, X., Chen, C., Kong, L., Wang, G., 2020. Engineering geology of residual soil derived from mudstone in Zimbabwe. Eng. Geol. 277, 105785. http://dx.doi.org/10.1016/j.enggeo.2020.105785.

Zhao, B., Wang, J., Coop, M., Viggiani, G., Jiang, M., 2015. An investigation of single sand particle fracture using X-ray micro-tomography. Géotechnique 65 (8), 625–641. http://dx.doi.org/10.1680/geot.4.P.157.